Escherichia coli's physiology can turn membrane voltage dyes into actuators

L Mancini[1], G Terradot[1,*], T Tian[2,*], Y Pu[2], Y Li[2], CJ Lo[3], F Bai[2], and T Pilizota[1,+]

[*]**these authors contributed equally to this work**
[+]**Corresponding author:teuta.pilizota@ed.ac.uk**

ABSTRACT

The electrical membrane potential (V_m) is one of the components of the electrochemical potential of protons across the biological membrane (proton motive force), which powers many vital cellular processes, and V_m also plays a role in signal transduction. Therefore, measuring it is of great interest, and over the years a variety of techniques has been developed for the purpose. In bacteria, given their small size, Nernstian membrane voltage probes are arguably the favourite strategy, and their cytoplasmic accumulation depends on V_m according to the Nernst equation. However, a careful calibration of Nernstian probes that takes into account the trade-offs between the ease with which the signal from the dye is observed, and the dyes' interactions with cellular physiology, is rarely performed. Here we use a mathematical model to understand such trade-offs and, based on the knowledge gained, propose a general work-flow for the characterization of Nernstian dye candidates. We demonstrate the work-flow on the Thioflavin T dye in *Escherichia coli*, and identify conditions in which the dye turns from a V_m probe into an actuator.

Keywords: Nernstian probes, single-cell microscopy, *Escherichia coli*

SIGNIFICANCE STATEMENT

The phospholipid bilayer of a biological membrane is virtually impermeable to charged molecules. Much like in a rechargeable battery, cells harness this property to store an electrical potential that fuels life reactions but also transduces signals. Measuring this electrical potential, also referred to as membrane voltage, is therefore of great interest and a variety of techniques have been employed for the purpose, starting as early as the 1930s. For the case of bacteria, which are smaller in size and possess a stiffer cell wall, arguably the most popular approach to measuring membrane voltage are Nernstian probes that accumulate across the bacterial membrane according to the Nernst potential. The present study characterizes the undesired effects Nernstian probes can have on cell physiology, which can be crucial for the accurate interpretation of experimental results. Using mathematical modelling and experiments, the study provides a general, simple workflow to characterise and minimise these effects.

INTRODUCTION

Living cells maintain an electric potential difference (V_m) across the plasma membrane that acts like a capacitor, and is achieved by active transport of ions:

$$V_m = F \cdot \frac{Q_{in}}{C} \tag{1}$$

where Q_{in} is the intracellular charge (in mole), C the membrane capacitance and F the Faraday constant. Membrane potential stands at the basis of fundamental biological processes, such as signal transduction and energy production [Del Castillo and Katz, 1954, Mitchell, 1961]. For the latter, V_m adds up to the chemical potential of protons, arising from their concentration difference across the membrane, to result in the proton electrochemical gradient, so called proton motive force (PMF). The PMF drives numerous cellular processes, most notably the production of ATP [Mitchell, 1961], import of nutrients or osmolites [Bradbeer, 1993, Jahreis et al., 2008, Ramos and Kaback, 1977, Wood, 2015] rotation of the bacterial flagellar motor [Sowa and Berry, 2008], and it is necessary for cell division [Strahl and Hamoen, 2010].

The notion that V_m lies at the very basis of life motivated decades long efforts to measure it. The first technique dates to 1939 and relies on the mechanical insertion of microelectrodes into squid giant axons [Hodgkin and Huxley, 1939]. The method was later applied to neurons [Ling and Gerard, 1949], and led to the development of the patch-clamp technique, which advanced the understanding of neuron signal transduction [Neher and Sakmann, 1976, Sakmann and Neher, 1984]. However, applicability of microelectrodes for the measurement of bacterial V_m is limited, owing to the small size of the organisms and the presence of the cell wall [Martinac et al., 1987, 2013]. Some of the subsequently developed methods overcome such limits with the use of molecular sensors [Felle et al., 1980], grouped in two categories: conformational-change-based sensors and Nernstian sensors. The former are static molecules or proteins that sit inside the membrane, or in its close proximity, and change conformation or electron distribution in response to changes in V_m, which in turn affect the optical properties of the chromophores thus transducing signal [Fluhler et al., 1985, Kralj et al., 2011, Tsutsui et al., 2008]. Here we focus on the latter, the Nernstian sensors, and on the parameter range in which they serve as V_m indicators, using *Escherichia coli* as the model organism.

Nernstian sensors are charged molecules that can diffuse across the biological membranes and distribute according to the Nernst equation:

$$V_m = \frac{RT}{zF} \ln\left(\frac{c_{out}}{c_{in}}\right) \tag{2}$$

where R, T, z, F, c_{out}, c_{in} denote respectively gas constant, temperature, valence of the charged molecule, Faraday's constant, external and internal concentration of the charged molecule. For a measurement to be attained, these molecules need to emit a signal that is a proxy for their number. Therefore, Nernstian V_m dyes are usually radio-labeled or fluorescent molecules [Felle et al., 1980, Sims et al., 1974], and V_m is calculated from equation (2) by measuring the cytoplasmic (c_{in}) and the external dye concentration (c_{out} [Lo et al., 2007].

However, Nernstian dyes are used in complex biological systems and a number of factors can be responsible for an incomplete adherence to a fully Nernstian behavior. In Fig. 1 we give a cartoon representation of the trade-offs imposed on a Nernstian dye by plotting the dye intensity inside *E. coli's* cytoplasm against the time. The chosen dye concentration should be such that the signal is sufficiently above the background (ΔI is sufficiently large). Yet, with increasing dye concentration, cell's V_m is more likely to be affected by the dye. This caveat is inherent to positively charged dyes as these directly lower V_m and more so at higher concentrations [Kashket, 1985]. The first requirement for a Nernstian dye is, thus, existence of a range of concentrations that give sufficient signal without extensively affecting the V_m. Likewise, cellular processes should not interfere with the Nernstian behavior of the dye, for example by actively importing or exporting it. Instead, the dye should be able to diffuse across the membrane and its diffusion constant will determine the time it takes for the dye to equilibrate across the membrane in agreement with equation (2) (τ_{eq} in Fig. 1). All phenomena that occur quicker than τ_{eq} are beyond the dye's temporal resolution, and likewise, all the measurements taken before τ_{eq} do not faithfully report V_m. Lastly, for quantitative measurements, Nernstian dyes should exhibit a well defined and constant correlation between the concentration and the signal, e.g. the dye should not self-quench at any point [te Winkel et al., 2016] or undergo signal enhancements.

To summarize, to be used as a Nernstian sensor, a cationic dye should: (i) give a sufficiently high signal without affecting cell's V_m; (ii) diffuse through the membrane with τ_{eq} on the order of minutes; (iii) stay inert, despite being charged, and not form bonds or in any way interact with cell; (iv) have constant signal per molecule. Yet, when using such dyes these requirements are rarely assessed in a systematic manner before measurements commence. In this work we identify a work-flow that should be adopted in order to identify the parameter range in which Nernstain dyes act as sensors, rather than actuators. We start with a mathematical model that helps us understand relationships and define trade-offs between dye working concentration and signal intensity, equilibration time and V_m perturbation. We then show how the identified work-flow can be used to benchmark new Nernstian dyes by characterizing the recently reported dye Thioflavin T (ThT) used in *Bacillus subtilis* [Prindle et al., 2015], for use in *E. coli*. We describe the physiological range in which ThT enables V_m sensing in *E. coli*, and, in the range where we find it turns into an actuator, we investigate the mechanistic reasons. Our work-flow can be applied to the characterization of other Nernstian dyes and provide novel insights for the established ones.

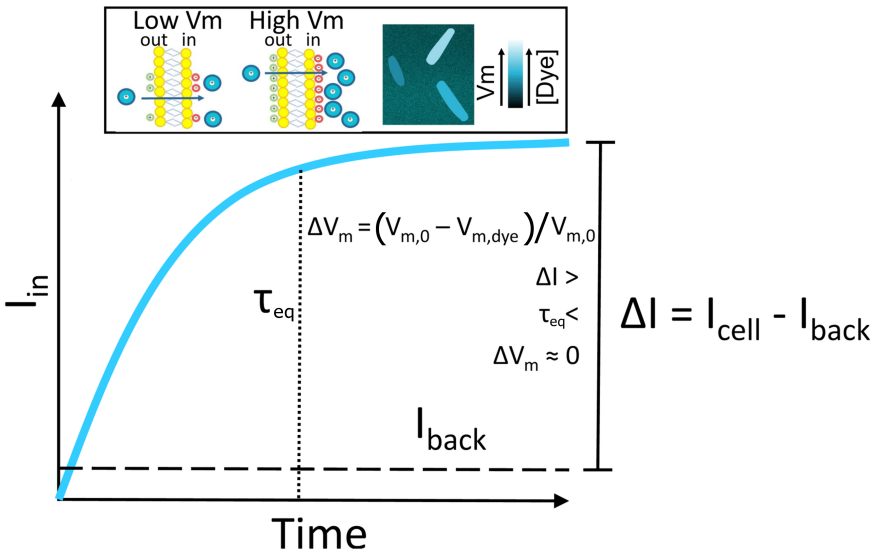

Figure 1. A schematic plot of a Nernstian dye equilibration curve. Equilibration time, τ_{eq}, is defined as the time at which the internalized dye I_{in} reaches the 90% of its final value. $V_{m,0}$ and $V_{m,dye}$ indicate the membrane potential before and after the addition of the dye, respectively. Inset: cartoon showing the mechanism of accumulation of cationic dyes, which accumulate more in cells with a highly negative V_m.

METHODS

Bacterial strains

All experiments where no mutation is explicitly indicated were carried out in the MG1655 strain. For the BFM speed assay we used MG1655 carrying the FliCsticky mutation from [Krasnopeeva et al., 2018]. Δ*tolC* mutants were obtained from the Keio collection [Baba et al., 2006]. Kanamycin resistance of the Keio deletion strain was removed via one-step inactivation with the plasmid pCP20 [Datsenko and Wanner, 2000]. Kanamycin resistance inactivation and elimination of the pCP20 plasmid were confirmed via Kanamycin, Chloramphenicol and Ampicillin sensitivity tests. Both the strain carrying the Δ*tolC* mutation and MG1655 wild-type were transformed with plasmid pTP20-mKate2 (Fig. SI9) for cytoplasmic volume measurements. pTP20-mKate2 contains the red fluorescent protein mKate2 and the ribosomal binding site (RBS) of mCherry. The plasmid was constructed as follows: the backbone from pWR20 [Pilizota and Shaevitz, 2012] and the sequence containing the RBS of mCherry and mKate2 were PCR amplified. The products were purified, cleaved with the restriction enzymes AvrII and NotI (NEB, UK) and ligated using T4 DNA ligase (Promega, UK). Chemically competent cells were transformed with the ligation mixes and transformants were confirmed by colony PCR and subsequently sequenced. A map of the plasmid and the primers are given in SI (Fig. SI9, and Table SI1). All the strains used in the study are summarized in the Table SI2.

Bacterial growth conditions

Cells for fluorescence microscopy were grown from an overnight culture by diluting it 1:80 times in LB (0.5% Yeast Extract, 1% Bacto tryptone, 0.5% NaCl). The culture was shaken at 220 rpm at 37°C and harvested at OD_{600}=0.3-0.5. Upon harvest we washed the cells into fresh LB or MM9 + glucose medium (50mM Na_2HPO_4, 25mM NaH_2PO_4, 8.5mM NaCl, 18.7mM NH4Cl, 0.1mM $CaCl_2$, 1mM KCl, 2mM $MgSO_4$, 1x MEM essential amino acids (Gibco, UK) and 0.3% glucose). For the simultaneous BFM speed and ThT fluorescence measurements cells were grown from an overnight culture by diluting it 1:80 times in TB (1% Bacto tryptone, 0.5% NaCl) at 200 rpm and 30°C. Cells were harvested at OD_{600}=0.8 as before [Rosko et al., 2017] and washed to fresh MM9 via centrifugation. Growth curves were obtained in a Spectrostar Omega microplate reader (BMG, Germany) using a flat-bottom 96-well plate that was covered with a lid during the experiments (Costar, UK). Each well contained 200μl of growth media, either MM9 + glucose or MM9 + glycerol (50mM Na_2HPO_4, 25mM NaH_2PO_4, 8.5mM NaCl, 18.7mM NH4Cl, 0.1mM $CaCl_2$, 1mM KCl, 2mM $MgSO_4$, 1x MEM essential aminoacids (Gibco, UK) and 0.3%

glycerol), and was inoculated with 2μl (1:100 dilution) of an overnight culture. Plates were grown at 37°C with 300 rpm shaking (double orbital mode) . ThT (Acros organics, USA) solutions were prepared from a 10 mM stock of ThT in water made at least monthly and stored at 4°C in the dark.

Fluorescence microscopy

Imaging was carried out in a custom-built microscope with a 100x oil immersion objective lens (Nikon, Japan), Neutral White LED as a source of illumination (Cairn Research Ltd, UK) and images were taken with an iXon Ultra 897 EMCCD camera (Andor, UK) [Krasnopeeva, 2018, Rosko, 2017]. ThT fluorescence was measured with ZET436/20x and ET525/40m, and mKate2 and PI fluorescence with ET577/25x and ET632/60m (Chroma Technology, USA) excitation and emission filters, respectively. Exposure time was 50 ms and Andor camera gain 25. We note that ThT undergoes a spectral shift and intensity increase when highly concentrated or when spatially constricted, either by binding to amyloid fibrils or by viscosity [Maskevich et al., 2015, 2007, Sulatskaya et al., 2017]. Our choice of filters aims at minimizing these effects and the damage that shorter wavelengths cause to *E. coli* [Vermeulen et al., 2008]. Cells were imaged in a custom-built flow-cell (Fig. SI10, [Krasnopeeva et al., 2018]), and attached to the coverslip surface as before [Krasnopeeva et al., 2018, Rosko et al., 2017]. Briefly, 1% Poly-L-Lysine (Sigma, UK) is flushed through the flow cell and washed with 3-5 ml of growth media after 10 s. Polystyrene particles (beads) with a diameter of 1 μm (Bangs Laboratories, USA), were delivered into the flow-cell and allowed to attach to the coverslip surface. After 10 min unattached beads were flushed away with 1-2 ml of growth media. Next, 200 μl of cells were delivered to the flow-cell and allowed to attach for 10-30 min, after which the unattached cells were removed with 1 ml of growth medium. 10 μM ThT in growth media was delivered with a peristaltic pump (Fusion 400, Chemyx, USA) using 50 μl/min flow rate while imaging. We deliver 5 μM of PI stain (MP Biomedicals, USA) in the same way. 5mM PI stock solution (in water) was stored at 4°C in the dark. Images were stabilized in x, y and z position using a bead attached to the cover-slip and back-focal-plane interferometry [Buda et al., 2016, Pilizota and Shaevitz, 2012].

Motor speed measurements

Single motor speeds were measured as before [Krasnopeeva et al., 2018, Rosko et al., 2017]. Briefly, we sheared flagellar filaments by passing them through two syringes with narrow-gauge needles (26 gauge) connected by plastic tubing. The cell attachment protocol was as above, except 0.5 μm beads (Polysciences, USA) were delivered after cell attachment allowing them to attach to filament stubs. Motor speed was measured during continuous flow that delivered MM9 + glucose medium supplemented with 10 μM ThT. Back-focal-plane interferometry setup and recording conditions are as before [Rosko et al., 2017].

Data analysis

Motor speed traces

Raw traces of the position of the bead attached to the filament stub were analyzed by a moving-window discrete Fourier transform as in [Rosko et al., 2017]. From the obtained motor speed traces DC frequency (50 Hz) was removed, speeds lower then 5 Hz ignored, and subsequently a median filter (window size 11) was applied [Krasnopeeva et al., 2018]. We note that we use a wild type strain for which the BFM can change rotational direction, which appears as a negative speed after application of the moving-window Fourier transform. However, for the purpose of PMF measurements these short intervals can be disregarded, and we only show the speed values above 0 Hz.

Fluorescence images

The image analysis was carried out with a custom written software. From fluorescence images, rectangles containing 'flat' cells, i.e. cells that are uniformly attached to the coverslip surface, as well as background rectangles within each cell-containing rectangle, were manually selected [Buda et al., 2016, Pilizota and Shaevitz, 2012]. The edge of the cell was identified within the cell-containing rectangle by applying a global threshold via the Otsu's method [Otsu, 1979]. To total cells' intensity values were obtained by summing up and averaging pixel belonging to the cells. Values obtained from the background rectangles at the time points when ThT was loaded in the channel but cells had not taken it up yet, were subtracted from the cell intensity values. The beads used for image stabilisation stain easily with ThT, and were used as a point of reference for dye entry (which in our case occurred 7 to 10 min from the start of

imaging). We show fluorescence intensity traces that start at the point of ThT entry, but note that cells were exposed to fluorescence illumination in the 7-10 min interval before. For the low fluorescence values characteristic of the early stages of dye equilibration, our script fails to identify cells, in which case we linearly interpolate values between two closest events of successful cell identification. Cell area was measured from intensity profiles, by normalizing them and counting the pixels above 30% of maximum intensity as described previously [Buda et al., 2016, Pilizota and Shaevitz, 2012]

Plate reader data

Individual growth curves were analysed with the software deODorizer from [Swain et al., 2016]. To extract the maximum growth rate, 3 or more repeats in the same condition were aligned by the chosen OD value (usually OD$\sim$0.4) using the growth curve that reached it first (in the given condition). The maximum growth rates given in Fig. 3C were normalized by the maximum growth rate in $[\mathrm{Dye}]_{out}$=0 condition.

RESULTS

Mathematical model of Nernstian dye's behavior defines its working parameter range

To predict and understand the mutual effects of dye concentration and cell physiology we turn to a mathematical model. We assume that the cytoplasmic and extracellular liquids are electrical conductors separated by the membrane, which we treat as a parallel-plate capacitor (equation 1) [Grabe and Oster, 2001]. We account for four types of charge carriers and assume that all are monovalent to simplify the model without altering the results with respect to V_m dye behavior: *(i)* negatively charged molecules to which the membrane is close to non-permeable denoted Y, *(ii)* cationic species actively pumped outward denoted C^+, *(iii)* anionic species, which equilibrates across the membrane A^- and *(iv)* cationic species that equilibrate across the membrane playing the part of a cationic dye. Thus Q_{in} is:

$$Q_{in} = V_{Cell} \cdot \left([Dye]_{in} + [C^+]_{in} - [A^-]_{in} - [Y]_{in}\right) \tag{3}$$

where V_{cell} is the intracellular volume. The extracellular concentrations and $[Y]_{in}$ are constants set by the initial conditions (we assume that the cell does not affect the ionic composition of its environment and we treat $[Y]_{in}$ as unable to cross the membrane). We also note that $[Dye]_{in}$ and $[Dye]_{out}$ are experimentally determined from fluorescence intensity signal, thus when presenting experimental results we use I_{in} and I_{out} instead.

The charge separation, and so V_m, is achieved in two ways. First, by pumping C^+_{in} outwards and thus creating an overall negatively charged intracellular environment, and second by maintaining $[Y]_{in}$ (an example of $[Y]_{in}$ is glutamate). We set the free-energy for the outward pumping of C^+ against its electrochemical gradient to be a constant, and label it ΔG_E (where $\Delta G_E < 0$). For example, in the case of a proton:ion antiporter with 1:1 exchange stoichiometry the free energy is the PMF itself, and for a similar antiporter with 2:1 proton:ion stoichiometry it is $2 \times$ PMF.

The rate at which C^+ is pumped out of the cell is $j_P = k_P \cdot \left(1 - e^{\Delta G_P/(RT)}\right)$, where k_P is a function that describes the specifics of the transport mechanism by a given pump, here, we keep it a constant. ΔG_P depends on the electrochemical potential of the pumped cation (ΔG_{C^+}) and ΔG_E. The chosen functional dependency of j_P gives the simplest pump kinetics, sufficient for our purpose, which can be expanded to include more complex pumping scenarios Keener and Sneyd [2009]. Therefore, the rate of pumping (positive flux means C^+ is extruded) depends on the intracellular ionic composition via V_m and $[C^+]_{in}$:

$$j_P = k_P \cdot \left(1 - e^{\Delta G_P/(RT)}\right) \tag{4}$$

$$\Delta G_P = \Delta G_E - \Delta G_{C^+} \tag{5}$$

$$\Delta G_{C^+} = F \cdot V_m + RT \cdot \ln\left(\frac{[C^+]_{in}}{[C^+]_{out}}\right) \tag{6}$$

Note that in order for the pump to move C^+ outward $j_P > 0$, and consequently $\Delta G_E < \Delta G_{C^+}$, i.e. the free-energy providing reaction has to be able to overcome the electrochemical gradient of the C^+.

Finally, the dye, the anion and the cation leak through the membrane (positive flux means x is moved inward) at the rate:

$$j_{L,x} = k_{L,x} \cdot \left(1 - e^{\Delta G_x/(RT)}\right), x \in \{Dye, C^+, A^-\} \tag{7}$$

$$\Delta G_x = F \cdot V_m + RT \cdot \ln\left(\frac{[x]_{in}}{[x]_{out}}\right) \tag{8}$$

Similarly to k_P, $k_{L,x}$ is a function whose shape depends on the mechanisms by which an ion leaks across the *E. coli* membrane, which in turn depends on the electrostatic potential at a position z within the membrane, $V(z)$. To the best of our knowledge, $V(z)$, and consequently $dV(z)/dz$, are not known for *E. coli*. We chose Eyring's model that has been verified for cationic leakage across the mitochondrial membrane [Garlid and Paucek, 2003], and which assumes $V(z)$ abruptly changes in the middle of the lipid bilayer, such that $dV(z)/dz = 0$ everywhere but at the geometrical middle of the membrane where $dV(z)/dz = V_m$ [Garlid et al., 1989]. We then have:

$$k_{L,x} = \frac{S_{cell}}{V_{cell}} \cdot P_x \cdot [x]_{out} \cdot e^{-\frac{F \cdot z_x \cdot V_m}{2 \cdot RT}}, \text{ with } x \in \{Dye, C^+, A^-\} \tag{9}$$

where S_{cell} denotes the cell's surface area and P_x the permeability of the membrane for $x \in \{Dye, C^+, A^-\}$. At steady-state *Dye* and A^- equilibrate across the membrane according to Nernst equation ($d[Dye]_{in}/dt = j_{L,Dye} = 0 \Leftrightarrow \Delta G_{Dye} = 0$, leading to (2)), whereas for the monovalent cation $d[C^+]_i/dt = 0 \Leftrightarrow j_{L,C^+} = j_P$. Next we introduce a new variable ("*pump-leak ratio*") defined as:

$$\rho = k_P/k_{L,C^+} = k_P \cdot \frac{V_{cell}}{S_{cell} \cdot P_{C^+} \cdot [C^+]_{out}} \cdot e^{\frac{F \cdot V_m}{2 \cdot RT}} \tag{10}$$

and re-write the steady-state condition for C^+ as:

$$\left(1 - e^{\Delta G_{C^+}/(RT)}\right) = \rho \cdot \left(1 - e^{(\Delta G_E - \Delta G_{C^+})/(RT)}\right) \tag{11}$$

Given a certain extracellular composition ($[Dye]_{out}$, $[C^+]_{out}$ and $[A^-]_{out}$), and taking into account that $[Dye]_{in}$ and $[A^-]_{in}$ are defined by the Nernst equation at steady-state, equation (11) gives us a unique solution for steady-state V_m for a set of $\{[Y]_{in}, \rho, \Delta G_E\}$ values.

We note from Eq. (11) that changing the functional dependency of $k_{L,x}$ or k_P does not affect how the steady-state V_m depends on ρ. However, the steady-state potential after addition of the dye relative to the steady-state potential in absence of the dye ($\Delta V_m = (V_{m,0} - V_{m,Dye})/V_{m,0}$) does. Similarly, the dynamics of dye equilibration are dependent on the functional dependency of $k_{L,x}$, k_P, *e.g.* assuming Goldman–Hodgkin–Katz flux equation Goldman [1943] instead of Erying's model for $k_{L,x}$ will give a slightly different dye equilibration profile (Fig. SI1). However, such changes will not influence the conclusions we reach based on our model predictions, because we are interested in the changes of the intracellular dye concentration dynamics at, e.g. different extracellular dye concentrations, $V_{m,0}$ or P_{Dye}. These partial derivatives of the intracellular dye concentration are invariant to the choice of $k_{L,x}$ and k_P.

Having constructed the model, we obtain the computational data in Fig. 2 in two steps. In the first step we allow the ODE system described by Eqs. SI 20, 21 to reach the steady-state ($V_{m,0}$) for a 3-D grid of $\{[Y]_{in}, \rho, \Delta G_E\}$. We note that in this step we do not need to specify ions' permeabilities nor the rate function for leakage $k_{L,x}$, because we define the values of ρ, which is the ratio of the two. We then use the obtained $V_{m,0}$ as the initial condition for the second step of the numerical experiment, which requires us to specify: *(i)* the rate function for leakage (Eq. (9)), *(ii)* the permeability of the membrane to the dye P_{Dye} and *(iii)* the concentration of the dye in the extracellular space $[Dye]_{out}$.

As increasing the $[Dye]$ gives better signal-to-noise ratio, we first look at the dye equilibration profile ($[Dye]_{in}$) for fixed $V_{m,0}$, $[Y]_i = 150$ mM, $\Delta G_E = -210$ mV and at different external dye concentrations ($[Dye]_{out}$). As expected, Fig. 2A shows that increasing $[Dye]_{out}$ improves the signal-to-noise ratio and shortens τ_{eq}, but at the same time increasingly depolarizes the membrane. The extent by which ΔV_m drops does not solely depend on the $[Dye]_{out}$, but also on the initial $V_{m,0}$. Fig. 2B shows dye equilibration profile

for a fixed $[Dye]_{out}$, but for different $V_{m,0}$ indicating that highly polarized cells are more susceptible to V_m loss. Apart from the value of $V_{m,0}$, ΔV_m will also depend on the charged permeable and non-permeable species that are generating it, as shown in Fig. SI2. If a given $V_{m,0}$ value is generated in the presence of a higher concentration of charged, impermeable intracellular species or at a higher energetic cost, ΔV_m will increase for the same $[Dye]_{out}$. Thus, the extent to which a given $[Dye]$ becomes and actuator and affects the ΔV_m is context dependant. Furthermore, while increasing $[Dye]_{out}$ shortens τ_{eq} this is only the case when $V_{m,0}$ is affected, as seen in Fig. SI3. Lastly, we look at the dye equilibration profile for different permeabilities of the membrane to the dye (P_{Dye}) in Fig. 2C, and show that for higher P_{Dye} same concentration of the dye lowers $V_{m,0}$ more. Fig. SI4 shows τ_{eq} as a function of P_{Dye} for different $V_{m,0}$.

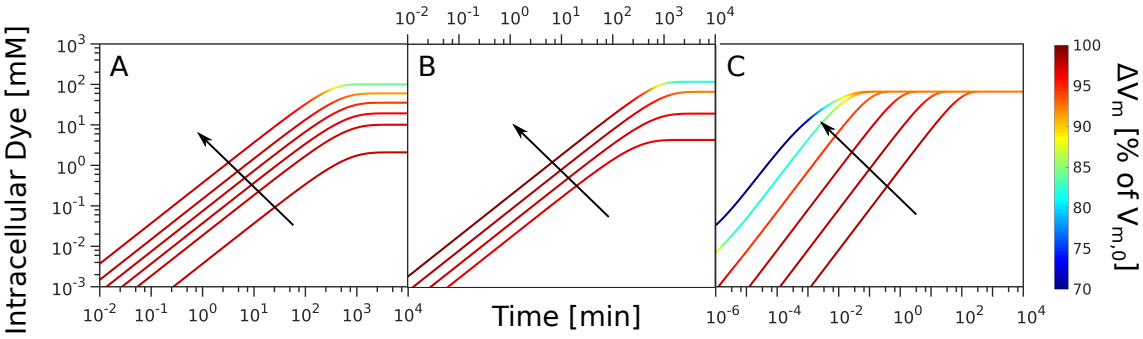

Figure 2. Computational data describing the parameter landscape associated with cationic dye usage as Nernstian sensors. (A) $V_{m,0} = -140$ mV, $Y_i = 150$ mM, $I_{Na} = 210$ mV. Intracellular Dye concentration as a function of time, for extracellular dye concentrations 10, 50, 100, 200, 400 and 1000 μM. The arrow indicated increasing $[Dye]_{out}$. (B) Extracellular dye concentration of 100 μM, $Y_i = 150$ mM, $\Delta G_E = -210$ mV. Intracellular dye concentration as a function of time, for different $V_{m,0}$: -220, -180, -140 and -100 mV. The arrow indicates increasing absolute value of the $V_{m,0}$. (C) $V_{m,0} = -180$ mV, $Y_i = 150$ mM, $\Delta G_E = -210$ mV, Extracellular dye at 100 μM. Intracellular dye concentration as a function of time, for different apparent permeabilities of the membrane to the dye: 10^{-12}, $10^{-10.8}$, $10^{-9.6}$, $10^{-8.4}$, $10^{-7.2}$, 10^{-6} meter per second. The arrow indicates increasing permeability.

The working concentration of Nernstain dye Thioflavin T for *E. coli* is in μm range

Guided by the model predictions we devise an experimental work-flow for assessing the parametric range in which a candidate cationic dye behaves like a Nernstian sensor, and choose Thioflavin T (ThT) for the purpose. ThT has recently been used as a V_m dye in *B. subtilis* [Prindle et al., 2015], but has not been characterized for use in *E. coli*. We start by identifying the working concentration that gives sufficiently large signal, yet minimizes the membrane voltage perturbation, ΔV_m, and use the growth rate as a proxy for affected ΔV_m. Fig. 3A and B show *E. coli* growth curves in MM9 media supplemented with glucose or glycerol respectively (see *Materials and Methods* for detailed media composition), and in the presence of a range of ThT concentrations. Fig. 3C shows growth rates plotted against the ThT concentration for both media, demonstrating that 10 μM ThT or less does not significantly affect the growth rate in either media. We call this concentration MNC (Maximum Non-inhibitory Concentration). However, the growth rate reduction observed for higher ThT concentrations is media dependent (Fig. 3C). The result is consistent with the finding of our model that the effect of the dye on cell's physiology is environment dependent.

We next check that the highest ThT concentration, which does not affect the growth rate (MNC), 10 μM, gives sufficiently high signal-to-noise ratio by observing the dye equilibration in different media. We note that if sufficient ΔI is achieved with 10 μM ThT we would further check that $\Delta V_m < 1\%$ by measuring the τ_{eq} with both 10 μM and a lower dye concentration. If $\Delta V_m < 1\%$, we expect τ_{eq} not to change based on the results of our model (Fig. 2A). Fig. 3D shows I_{in} in time in LB and Fig. 3E the same in MM9 media supplemented with glucose. In both cases fresh media with ThT is continuously supplied using a customized flow-cell (see *Materials and Methods*), and in both cases ΔI is sufficiently high. However, observed profiles are different from expected (Fig. 1), and show a characteristic initial peak and a final plateau (SI Video 1). We reasoned that the peak could either be a real fluctuation in V_m or it could indicate an unknown dye export mechanism.

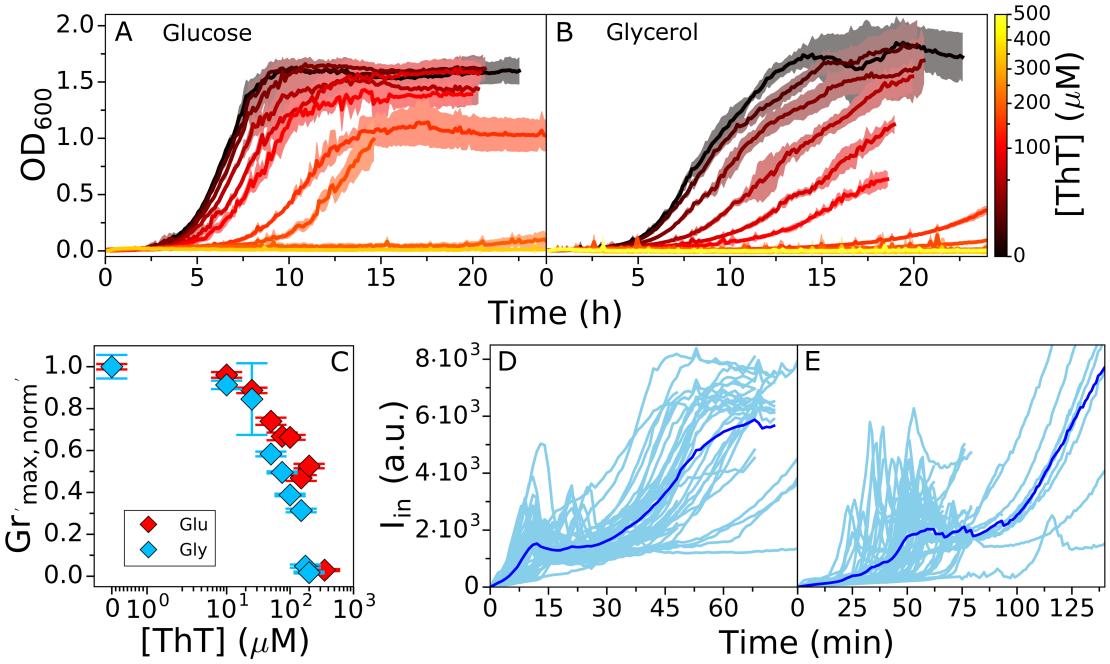

Figure 3. *E. coli* growth in the presence of ThT. *E. coli* growing in MM9 media supplemented with (A) glucose or (B) glycerol at increasing ThT concentration (colourmap). ThT concentrations in (A) are 10, 25, 50, 75, 100, 200, 350 μM and in (B) 10, 25, 50, 75, 100, 150, 175, 200 μM). The error bars are standard deviations. (C) Maximum growth rates from (A) and (B) for each ThT concentration are given in red and blue respectively. Each condition was done at least in triplicate and error bars are the standard deviation. (D) I_{in} against time in LB and in (E) MM9 + glucose media. Individual cells are shown in cyan (45 in (D) and 52 in (E) from at least 9 independent experiments), and the average trace is shown in blue. The imaging conditions and $I_{ex} = 10\mu M$ are the same for (E) and (D).

Multi-drug efflux pumps influence ThT accumulation in *E. coli*

To determine whether the observed peak in I_{in} is due to active export of the dye we first check that in *E. coli* ThT is not a multi-drug-efflux pump substrate. We are motivated by previous reports that show that dyes such as ethidium bromide and Nile red are substrates of pumps belonging to the five bacterial structural families: ABC (ATP-binding cassette), RND (resistance/nodulation/division), MATE (multidrug and toxic compound extrusion), MFS (major facilitator superfamily) and SMR (small multidrug resistance) [Alvarez-Ortega et al., 2013, Bay et al., 2008, Kuroda and Tsuchiya, 2009, Lubelski et al., 2007, Nikaido and Takatsuka, 2009]. Fig. 4A shows dye equilibration curves in a wild type (WT) strain compared to the strain bearing a deletion of TolC, which is a gene encoding for an outer membrane protein (OMP) that is a ubiquitous component of multi-drug efflux pumps [Anes et al., 2015]. The I_{in} peak in the deletion mutant did not disappear, instead the intensity level of the peak was even higher, suggesting the pump is involved in the dye export, but also that the qualitative difference between the expected and the observed equilibration curve shape is not due to dye export. Interestingly, in the mutant, the peak also occurred earlier in time during the loading and with less cell-to-cell variability. We next tested the effect of the ThT dye on the Δ*TolC* mutant growth rates, Fig. 4B. We found that at the MNC for the WT, the mutants' growth was inhibited over the course of our experiment. Taken together the results indicate that ThT is likely pumped out of the cells by one or more types of TolC-dependent efflux pumps, thereby preventing its use for quantitative V_m measurements in WT *E. coli*.

Changing the membrane permeability during ThT loading can lead to loss of V_m

We next tested our second hypothesis that the I_{in} peak is due to a decrease in V_m. To this end, we performed measurements of bacterial flagellar motor (BFM) speed [Krasnopeeva et al., 2018] during ThT loading. BFM is a rotary molecular motor roughly 50 nm in size that enables bacterial swimming [Sowa and Berry, 2008] via PMF driven rotation [Fung and Berg, 1995, Manson et al., 1980, Matsuura

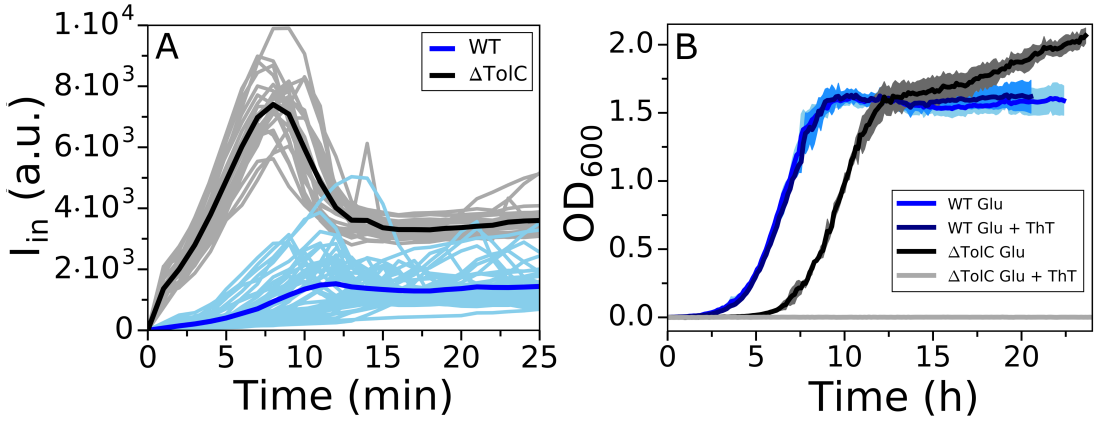

Figure 4. Comparison of WT and ΔTolC mutant response to ThT. (A) I_{in} versus time for the WT (cyan) and ΔTolC (gray) loaded in LB. WT traces are reproduced from Fig. 3D and ΔTolC traces were obtained from 5 independent experiments to give 23 single cell traces. Averaged traces for the WT and ΔTolC are given in blue and black respectively. (B) Growth curves of WT and ΔTolC in MM9 + glucose media are given in blue (reproduced from Fig. 3A) and black, respectively. Growth curves in the same media, but in the presence of 10 μM ThT, are given in cyan (WT) and gray (ΔTolC). The shaded areas show standard deviation and cyan and blue growth curves for the WT overlap.

et al., 1977, Meister and Berg, 1987]. The motor speed (ω) varies linearly with PMF [Fung and Berg, 1995, Gabel and Berg, 2003], which enables its use as a PMF, and when $pH_{in} = pH_{out}$, as a V_m indicator as well [Krasnopeeva et al., 2018]. In our conditions, pH_{out} is 7 and pH_{in} is 7.86 (Fig. SI5) making the contribution to the PMF from ΔpH ∼50 mV. Thus, even if during our experiment ΔpH goes to 0, we can learn about the V_m behaviour from the PMF measurements via the motor speed. We measure ω as before, using back-focal-plane interferometry [Svoboda et al., 1993] and a polystyrene bead attached to a short filament stub (see *Materials and Methods*) [Bai et al., 2010, Krasnopeeva et al., 2018, Rosko et al., 2017, Ryu et al., 2000].

Fig. 5A shows simultaneous measurements of ThT intensity and normalized motor speed during dye equilibration in MM9 + glucose. The motor speed decreases during ThT equilibration and BFM stops at the point of I_{in} decrease. Furthermore, BFM does not resume spinning even as I_{in} further increases, suggesting that the second ThT intensity increase that culminates in a plateau, is not driven by V_m. To confirm the result, during ThT equilibration, we supplemented the medium with propidium iodide (PI). PI permeates bacterial membrane that lost its integrity and significantly enhances its quantum yield upon binding to DNA, which is commonly interpreted as an indication of cell death [Krämer et al., 2016, Lopez-Amoros et al., 1995]. We found that the cells stained with PI although ThT intracellular concentration remained high, Fig. 5B. In addition, at the time point of I_{in} decrease cellular volume suddenly increases, and cytoplasmically expressed fluorescent protein mCherry-mKate2 hybrid (referred to as mKate2 for brevity) [Lord, 2014] starts leaking out of the cell, Fig. 5C, SI Video 2.

These results are in contradiction with our estimate of dye working concentration, and we wondered, based on Fig. 2C, if the changes in P_{Dye} could be the explanation. The cell culture in Fig. 3 was briefly exposed to light at 600 nm every 7.5 min, whereas cells in our flow-cell were exposed to light of 435 nm every minute for the purpose of imaging the ThT dye. We have previously reported loss of V_m and PMF due to light-induced decrease of *E. coli* membrane's resistance at effective powers higher than ∼ 17 mW/cm^2, and for a combination of 395 and 475 nm wavelengths [Krasnopeeva et al., 2018]. Light damage is wavelength dependent [Vermeulen et al., 2008], and we therefore characterized the light damage caused by our imaging conditions, i.e. 435 nm wavelength and effective power of $P_{eff} \sim 11$ mW/cm^2. Fig. SI7 shows a decrease in BFM motors' speed, and thus cell's PMF. However, the PMF is not fully lost, indicating that the loss of PMF observed in Fig. 5A is likely caused by the combination of light induced increase in P_{Dye} and exposure to 10 μM ThT.

To prove it, we exposed the bacteria to 10 μM ThT in LB as before, but this time we observe the cells under bright-field illumination for 45 min, at which point we turn on the 435 nm light used for epifluorescent imaging of ThT. Fig. 5E shows that after 45 min cells not exposed to 435 nm light did not

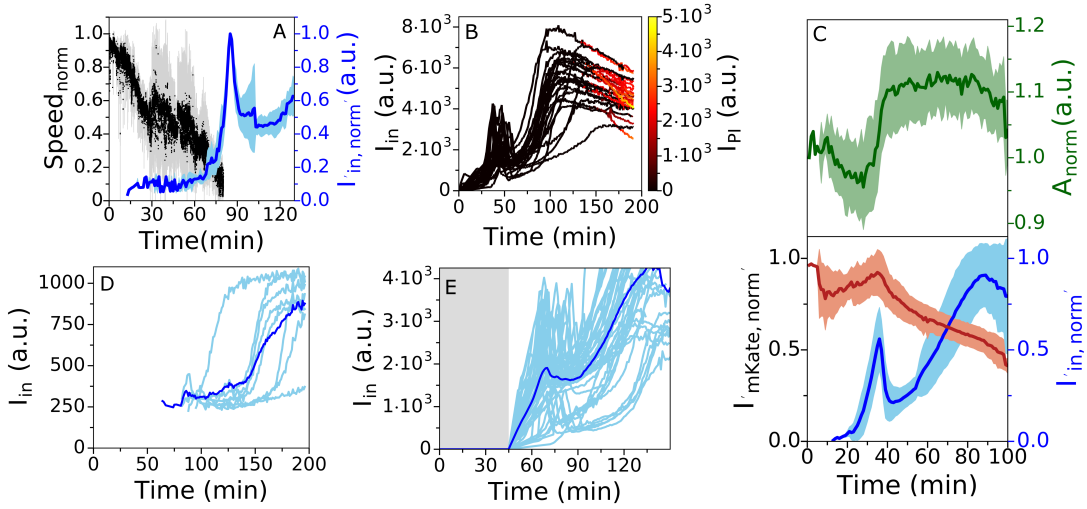

Figure 5. (A) Average traces of ThT fluorescence (in blue) and motor speed (in black) simultaneously measured in 5 individual cells (individual cell traces are given in Fig. SI6). The shaded areas show the standard deviation and the motor speed has been normalized to the initial value as described in *Materials and Methods*. (B) ThT (y axes) and PI (colourmap) equilibration profile in LB. 25 individual traces are given. (C) Average of ThT (in blue), mKate2 (in red) fluorescence and cell area (in green) simultaneously measured in 12 individual cells from 3 independent experiments. The shaded areas show the standard deviation. (D) Equilibration profile of 1 μM ThT in LB. 8 single cell traces and average trace are given in cyan and blue, respectively. (E) Equilibration profile of 10 μM ThT in LB in the absence (gray shaded area) and presence of epifluorescent illumination (light area). The dye was flown in the flow cell for the whole length of the experiment, imaging conditions in the light area were the same as in Figure 3 and 5D. 44 cells from 8 independent experiments are given.

take up ThT, in contrast to Fig.3D where cells exposed to 435 nm light from the start, took up ThT in the first 30 min.

Actively changing membrane permeability has been used to facilitate loading of Nernstian sensors [Lo et al., 2007], and Fig. 5E shows that this can change the dye into an actuator because it can influence V_m. Our mathematical model predicts that if a given concentration of the dye is lowering V_m, an even lower concentration of the dye will result in a change of τ_{eq} (Fig. SI3). In agreement, Fig. 5D shows that for 1 μM concentration of ThT τ_{eq} lasted longer then with 10 μM. Thus, 10 μM ThT in LB, under 435 nm light, affects V_m. Assessing the suitability of the dye working concentration by confirming that a lower dye concentration does not alter τ_{eq} is a suitable additional control we propose, especially if P_{Dye} is being altered as part of the experiments.

We note that in our plate reader experiments (Fig. 2) we observed the effect of the dye (above 10μM) on cell growth, while in our microscopy experiments, in the absence of light damage, ThT does not permeate WT cells. We thus wanted to confirm that at higher concentrations ThT permeates the cells and for the purpose we imaged the cells from the wells at representative ThT concentrations in MM9+glucose (10, 50 and 100 μM) and MM9+glycerol (10 μM). We found that in MM9 glucose cell brightness increases with the extracellular dye concentration and that in MM9+glycerol, at 10μM, ThT signal from the cells is overall greater that in glucose (Fig. SI8).

Having identified the mechanisms behind the shape of the ThT loading curve we observed in Fig. 3 we should now be able to reproduce it with our mathematical model. Based on Fig 5A we assume that V_m decays exponentially immediately after addition of the dye [Krasnopeeva et al., 2018]: $V_m(t) = V_{m,0} \cdot 2^{t/t_{1/2}}$ where $t_{1/2}$ is the time at which voltage is half that of $V_{m,0}$. The dynamics of dye entry are then modelled by Eyring's rate law Eq. (9) taking into account $V_{m,0}$, $t_{1/2}$ and P_{Dye} (see *Supplementary Information* for further details on the model). Fig. SI9 shows that the model reproduces the peak in $[Dye]_{in}$ observed in Fig. 3. Immediately upon addition, the positively charged dye moves inwards because its extracellular concentration is higher than the intracellular and the cell is negatively polarized. Thus, $[Dye]_{in}$ increases and becomes greater than $[Dye]_{out}$ until the electrochemical potential reaches $\Delta G_{Dye} = 0$ (at the peak).

As the V_m decays and since $[Dye]_{in} > [Dye]_{out}$, the dye now starts moving outwards and its intracellular concentration decreases. The time at which the peak occurs as well as its intensity depend on P_{Dye} as follows: *(i)* the time of the peak decreases with increasing P_{Dye} and increases with increasing $t_{1/2}$, and *(ii)* the intensity of the peak increases with increasing P_{Dye} and $t_{1/2}$, Fig SI9 C and D.

The dye still equilibrates according to equation (2), but this is achieved transiently at the time of the peak, which is the time point at which V_m can be calculated from equation (2). Since the V_m varies during the course of the experiment, the V_m measured at the peak is not equal to the $V_{m,0}$. Nonetheless, if we measure $V_m(t)/V_{m,0}$ as well as calculate the V_m at the time of the peak using eq. (2), in principle we can estimate $V_{m,0}$ as well. Thus, charged dyes can be used to estimate initial V_m even in conditions where they act as actuators and collapse V_m, if the dynamical shape of the V_m loss is known.

DISCUSSION

Nernstian probes are a popular choice for estimating bacterial V_m, because their concentration directly depends on V_m according to the Nernst equation. Despite the wide usage, the probes are often not sufficiently calibrated before use in different conditions. Here we present a mathematical model that shows trade-offs between requirements imposed on the dye: sufficient signal-to-noise ratio, sufficiently short dye equilibration time and minimum effect on the cells' physiology. Based on the model results we propose a general work-flow for the characterization of Nernstian dye candidates (Fig. 6), and demonstrate it on a newly suggested, and previously uncharacterized in *E. coli*, fluorescent dye Thioflavin T. We find that the suitability of a candidate Nernstian dye is context dependent, and reveal that the candidate dyes can be substrates for bacterial drug-export systems. We believe our work-flow is sufficiently simple and general to provide a common standard for benchmarking the cationic dye behavior and thus improve the robustness of V_m measurements.

We found as well that imaging conditions can affect how well the dye crosses bacterial membrane, which suggest that on its own *E. coli* membrane exhibits low permeability to this Nernstian sensor, or that its export by membrane efflux pumps is substantial. The observation is consistent with previous results that needed to permeabilize the membrane by EDTA to achieve experimentally reasonable loading times [Lo et al., 2007]. However, changing the membrane permeability is often not dye specific, and can lead to changes in the overall V_m of the cell. Our model suggests that if the chosen dye working concentration is not affecting V_m, lower dye concentration should leave τ_{eq} unchanged. The finding offers a simple test to confirm the suitability of the chosen dye working concentration, which should be performed in each environmental and physiological condition.

As a final remark, the fact that in the absence of illumination of shorter wavelengths, i.e. in our plate reader experiments, ΔTolC mutant is affected significantly more by the dye than the wild type suggest that, in the rich defined medium such as MM9 + glucose and amino acids, low cytoplasmic dye concentration is not just a consequence of low membrane permeability to the dye, but also of the active efflux. Then, in a condition where membrane permeability is affected, leading to the PMF loss, which is in turn the energy source for efflux pumps, the cytoplasmic concentration of the dye is no longer in accordance with equation (2) and could result in interesting dynamics such as in Fig. 5A, where we observe significant accumulation of the dye only after the PMF drops to a certain threshold value.

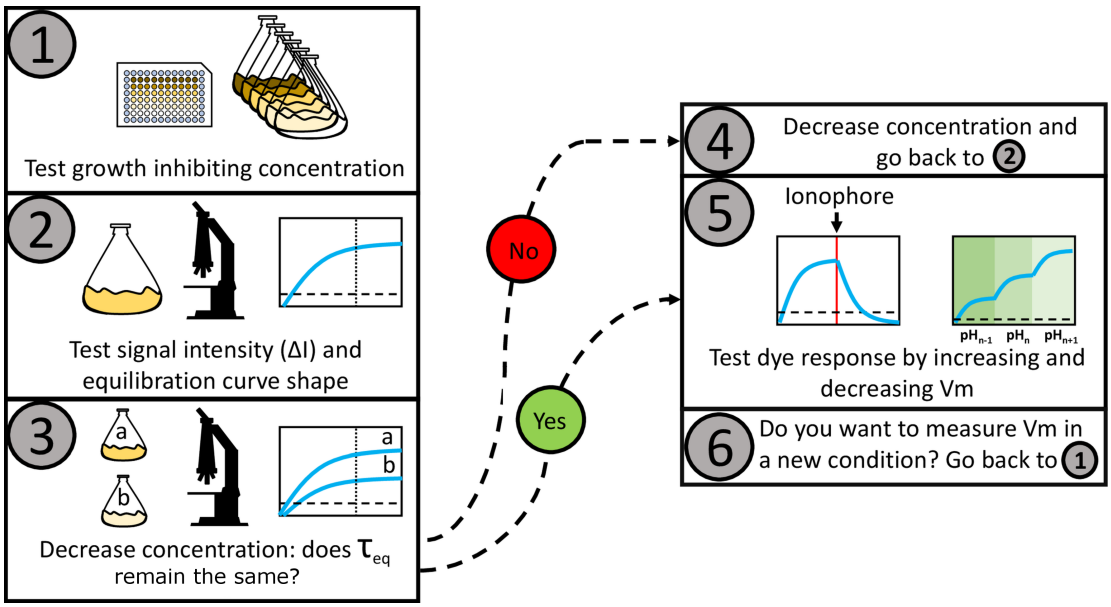

Figure 6. Proposed work-flow for characterizing the Nernstian behavior of a candidate cationic membrane voltage dye. The working concentration is estimated in steps 1 to 4, we define it as the maximum dye concentration that does not affect membrane voltage and that yields sufficient amount of signal. (1) The MNC is estimated. (2) The MNC is tested for sufficient signal intensity. (3) The effect of the dye on V_m is determined by measuring τ_{eq} at different below-MNC concentrations. (4) Different τ_{eq} for different dye concentrations indicate that the probe is altering V_m and the working concentration should be reduced and the protocol resumed from (2). Equal τ_{eq} indicates that the probe is not altering V_m. (5) Common procedures to test Nernstian dye responses can then be applied, such as the introduction of a ionophore that neutralizes V_m, or changes in external pH that induce changes in V_m [Lo et al., 2007]. (6) Because the effects depend on the physiological state of the cell, the procedure should be repeated for every experimental condition.

AUTHOR CONTRIBUTIONS

LM, GT, CJL, BF and TP conceived the experiments and the computational work. LM, TT, YP and YL performed experiments. GT performed computational work. LM analysed experimental data, and LM, GT, CJL, BF and TP interpreted the results and wrote the manuscript.

ACKNOWLEDGEMENTS

We thank Dario Miroli for help with image analysis, Nathan Lord and Sebastian Jaramillo-Riveri for donating us the construct containing the hybrid mCherry-mKate2 sequence and Angela Dawson for retrieving the ΔTolC mutant from the Keio collection. This work was financially supported by the Cunningham Trust scholarship ACC/KWF/PhD1 to TP and LM, the National Natural Science Foundation of China under grants No. 31722003 and No. 31770925 to FB, the Ministry of Science and Technology, Republic of China, under contract No. MOST-107-2112-M-008-025-MY3 to CJL and Human Frontiers Program grant RGP0041/2015 to TP, FB and CJL. TP acknowledges the support of UK Research Councils Synthetic Biology for Growth programme and is a member of the BBSRC/EPSRC/MRC funded Synthetic Biology Research Centre (BB/M018040/1).

REFERENCES

Alvarez-Ortega, C., Olivares, J., and Martínez, J. L. (2013). Rnd multidrug efflux pumps: what are they good for? *Front Microbiol*, 4:7–7. 23386844[pmid].

Anes, J., McCusker, M. P., Fanning, S., and Martins, M. (2015). The ins and outs of rnd efflux pumps in escherichia coli. *Front Microbiol*, 6:587–587. 26113845[pmid].

Baba, T., Ara, T., Hasegawa, M., Takai, Y., Okumura, Y., Baba, M., Datsenko, K. A., Tomita, M., Wanner, B. L., and Mori, H. (2006). Construction of escherichia coli k-12 in-frame, single-gene knockout mutants: the keio collection. *Molecular Systems Biology*, 2(1).

Bai, F., Branch, R. W., Nicolau, D. V., Pilizota, T., Steel, B. C., Maini, P. K., and Berry, R. M. (2010). Conformational spread as a mechanism for cooperativity in the bacterial flagellar switch. *Science*, 327(5966):685–689.

Bay, D. C., Rommens, K. L., and Turner, R. J. (2008). Small multidrug resistance proteins: A multidrug transporter family that continues to grow. *Biochimica et Biophysica Acta (BBA) - Biomembranes*, 1778(9):1814 – 1838. Structural proteomics of the cell envelope of Gram-negative bacteria.

Bradbeer, C. (1993). The proton motive force drives the outer membrane transport of cobalamin in *Escherichia coli*. *Journal of bacteriology*, 175(10):3146–50.

Buda, R., Liu, Y., Yang, J., Hegde, S., Stevenson, K., Bai, F., and Pilizota, T. (2016). Dynamics of escherichia coli's passive response to a sudden decrease in external osmolarity. *Proceedings of the National Academy of Sciences*, 113(40):E5838–E5846.

Datsenko, K. A. and Wanner, B. L. (2000). One-step inactivation of chromosomal genes in escherichia coli k-12 using pcr products. *Proceedings of the National Academy of Sciences*, 97(12):6640–6645.

Del Castillo, J. and Katz, B. (1954). Quantal components of the end-plate potential. *J Physiol*, 124(3):560–573. 13175199[pmid].

Felle, H., Porter, J. S., Slayman, C. L., and Kaback, H. R. (1980). Quantitative measurements of membrane potential in escherichia coli. *Biochemistry*, 19(15):3585–3590. PMID: 6996707.

Fluhler, E., Burnham, V. G., and Loew, L. M. (1985). Spectra, membrane binding, and potentiometric responses of new charge shift probes. *Biochemistry*, 24(21):5749–5755. PMID: 4084490.

Fung, D. C. and Berg, H. C. (1995). Powering the flagellar motor of escherichia coli with an external voltage source.

Gabel, C. V. and Berg, H. C. (2003). The speed of the flagellar rotary motor of escherichia coli varies linearly with protonmotive force. *Proceedings of the National Academy of Sciences*, 100(15):8748–8751.

Garlid, K. D., Beavis, A. D., and Ratkje, S. K. (1989). On the nature of ion leaks in energy-transducing membranes. *Biochimica et Biophysica Acta (BBA) - Bioenergetics*, 976(2):109 – 120.

Garlid, K. D. and Paucek, P. (2003). Mitochondrial potassium transport: the k+ cycle. *Biochimica et Biophysica Acta (BBA) - Bioenergetics*, 1606(1):23 – 41.

Goldman, D. E. (1943). Potential, impedance, and rectification in membranes. *The Journal of General Physiology*, 27(1):37–60.

Grabe, M. and Oster, G. (2001). Regulation of organelle acidity. *The Journal of General Physiology*, 117(4):329–344.

Hodgkin, A. L. and Huxley, A. F. (1939). Action Potentials Recorded from Inside a Nerve Fibre. *Nature*, 144:710.

Jahreis, K., Pimentel-Schmitt, E. F., Brückner, R., and Titgemeyer, F. (2008). Ins and outs of glucose transport systems in eubacteria. *FEMS Microbiology Reviews*, 32(6):891–907.

Kashket, E. R. (1985). The proton motive force in bacteria: A critical assessment of methods. *Annual Review of Microbiology*, 39(1):219–242. PMID: 2998266.

Keener, J. and Sneyd, J. (2009). *Mathematical Physiology*, page 93.

Kralj, J. M., Hochbaum, D. R., Douglass, A. D., and Cohen, A. E. (2011). Electrical spiking in escherichia coli probed with a fluorescent voltage-indicating protein. *Science*, 333(6040):345–348.

Krämer, C. E. M., Wiechert, W., and Kohlheyer, D. (2016). Time-resolved, single-cell analysis of induced and programmed cell death via non-invasive propidium iodide and counterstain perfusion. *Scientific Reports*, 6:32104 EP –. Article.

Krasnopeeva, E. (2018). *Single cell measurements of bacterial physiology traits during exposure to an external stress*. PhD thesis, University of Edinburgh.

Krasnopeeva, E., Lo, C.-J., and Pilizota, T. (2018). Single-cell bacterial electrophysiology reveals mechanisms of stress-induced damage. *arXiv*.

Kuroda, T. and Tsuchiya, T. (2009). Multidrug efflux transporters in the mate family. *Biochimica et Biophysica Acta (BBA) - Proteins and Proteomics*, 1794(5):763 – 768. Mechanisms of Drug Efflux and Strategies to Combat Them.

Ling, G. and Gerard, R. W. (1949). The normal membrane potential of frog sartorius fibers. *Journal of*

Cellular and Comparative Physiology, 34(3):383–396.

Lo, C.-J., Leake, M. C., Pilizota, T., and Berry, R. M. (2007). Nonequivalence of membrane voltage and ion-gradient as driving forces for the bacterial flagellar motor at low load. *Biophysical Journal*, 93(1):294 – 302.

Lopez-Amoros, R., Comas, J., and Vives-Rego, J. (1995). Flow cytometric assessment of escherichia coli and salmonella typhimurium starvation-survival in seawater using rhodamine 123, propidium iodide, and oxonol. *Applied and Environmental Microbiology*, 61(7):2521–2526.

Lord, N. (2014). *Fluctuation timescales in bacterial gene expression*. PhD thesis, Harvard University.

Lubelski, J., Konings, W. N., and Driessen, A. J. M. (2007). Distribution and physiology of abc-type transporters contributing to multidrug resistance in bacteria. *Microbiol Mol Biol Rev*, 71(3):463–476. 17804667[pmid].

Manson, M. D., Tedesco, P., and Berg, H. C. (1980). Energetics of flagellar rotation in bacteria. *Journal of Molecular Biology*, 138(3):541 – 561.

Martinac, B., Buechner, M., Delcour, A. H., Adler, J., and Kung, C. (1987). Pressure-sensitive ion channel in escherichia coli. *Proceedings of the National Academy of Sciences*, 84(8):2297–2301.

Martinac, B., Rohde, P. R., Cranfield, C. G., and Nomura, T. (2013). *Patch Clamp Electrophysiology for the Study of Bacterial Ion Channels in Giant Spheroplasts of E. coli*, pages 367–380. Humana Press, Totowa, NJ.

Maskevich, A. A., Lavysh, A. V., Kuznetsova, I. M., Sulatskaya, A. I., and Turoverov, K. K. (2015). Spectral manifestations of thioflavin t aggregation. *Journal of Applied Spectroscopy*, 82(1):33–39.

Maskevich, A. A., Stsiapura, V. I., Kuzmitsky, V. A., Kuznetsova, I. M., Povarova, O. I., Uversky, V. N., and Turoverov, K. K. (2007). Spectral properties of thioflavin t in solvents with different dielectric properties and in a fibril-incorporated form. *Journal of Proteome Research*, 6(4):1392–1401. PMID: 17305383.

Matsuura, S., ichi Shioi, J., and Imae, Y. (1977). Motility in bacillus subtilis driven by an artificial protonmotive force. *FEBS Letters*, 82(2):187 – 190.

Meister, M. and Berg, H. C. (1987). The stall torque of the bacterial flagellar motor. *Biophys J*, 52(3):413–419. 3651560[pmid].

Mitchell, P. (1961). Coupling of phosphorylation to electron and hydrogen transfer by a chemi-osmotic type of mechanism. *Nature*, 191:144 EP –.

Neher, E. and Sakmann, B. (1976). Single-channel currents recorded from membrane of denervated frog muscle fibres. *Nature*, 260:799 EP –.

Nikaido, H. and Takatsuka, Y. (2009). Mechanisms of rnd multidrug efflux pumps. *Biochim Biophys Acta*, 1794(5):769–781. 19026770[pmid].

Otsu, N. (1979). A threshold selection method from gray-level histograms. *IEEE Transactions on Systems, Man, and Cybernetics*, 9(1):62–66.

Pilizota, T. and Shaevitz, J. W. (2012). Fast, multiphase volume adaptation to hyperosmotic shock by escherichia coli. *PLOS ONE*, 7(4):1–10.

Prindle, A., Liu, J., Asally, M., Ly, S., Garcia-Ojalvo, J., and Süel, G. M. (2015). Ion channels enable electrical communication in bacterial communities. *Nature*, 527:59.

Ramos, S. and Kaback, H. R. (1977). The relation between the electrochemical proton gradient and active transport in escherichia coli membrane vesicles. *Biochemistry*, 16(5):854–859. PMID: 14665.

Rosko, J. (2017). *Osmotaxis in Escherichia coli*. PhD thesis, University of Edinburgh.

Rosko, J., Martinez, V. A., Poon, W. C. K., and Pilizota, T. (2017). Osmotaxis in escherichia coli through changes in motor speed. *Proceedings of the National Academy of Sciences*.

Ryu, W. S., Berry, R. M., and Berg, H. C. (2000). Torque-generating units of the flagellar motor of escherichia coli have a high duty ratio. *Nature*, 403:444 EP –.

Sakmann, B. and Neher, E. (1984). Patch clamp techniques for studying ionic channels in excitable membranes. *Annual Review of Physiology*, 46(1):455–472. PMID: 6143532.

Sims, P. J., Waggoner, A. S., Wang, C.-H., and Hoffman, J. F. (1974). Mechanism by which cyanine dyes measure membrane potential in red blood cells and phosphatidylcholine vesicles. *Biochemistry*, 13(16):3315–3330. PMID: 4842277.

Sowa, Y. and Berry, R. M. (2008). Bacterial flagellar motor. *Quarterly Reviews of Biophysics*, 41(2):103–132.

Strahl, H. and Hamoen, L. W. (2010). Membrane potential is important for bacterial cell division.

Proceedings of the National Academy of Sciences, 107(27):12281–12286.

Sulatskaya, A. I., Lavysh, A. V., Maskevich, A. A., Kuznetsova, I. M., and Turoverov, K. K. (2017). Thioflavin T fluoresces as excimer in highly concentrated aqueous solutions and as monomer being incorporated in amyloid fibrils. *Scientific Reports*, 7(1):1–11.

Svoboda, K., Schmidt, C. F., Schnapp, B. J., and Block, S. M. (1993). Direct observation of kinesin stepping by optical trapping interferometry. *Nature*, 365:721 EP –.

Swain, P. S., Stevenson, K., Leary, A., Montano-Gutierrez, L. F., Clark, I. B. N., Vogel, J., and Pilizota, T. (2016). Inferring time derivatives including cell growth rates using Gaussian processes. *Nature Communications*, 7:13766.

te Winkel, J. D., Gray, D. A., Seistrup, K. H., Hamoen, L. W., and Strahl, H. (2016). Analysis of antimicrobial-triggered membrane depolarization using voltage sensitive dyes. *Frontiers in Cell and Developmental Biology*, 4:29.

Tsutsui, H., Karasawa, S., Okamura, Y., and Miyawaki, A. (2008). Improving membrane voltage measurements using FRET with new fluorescent proteins. *Nature Methods*, 5(8):683–685.

Vermeulen, N., Keeler, W., Kanavillil, N., and Leung, K. (2008). The bactericidal effect of ultraviolet and visible light onescherichia coli. 99:550–6.

Wood, J. M. (2015). Bacterial responses to osmotic challenges. *The Journal of General Physiology*, 145(5):381–388.